Modulation of the MJO intensity over the equatorial western Pacific by two types of El Niño

Lu Wang, Tim Li, Lin Chen, Swadhin K. Behera & Tomoe Nasuno

Climate Dynamics
Observational, Theoretical and Computational Research on the Climate System

ISSN 0930-7575

Clim Dyn
DOI 10.1007/s00382-017-3949-6

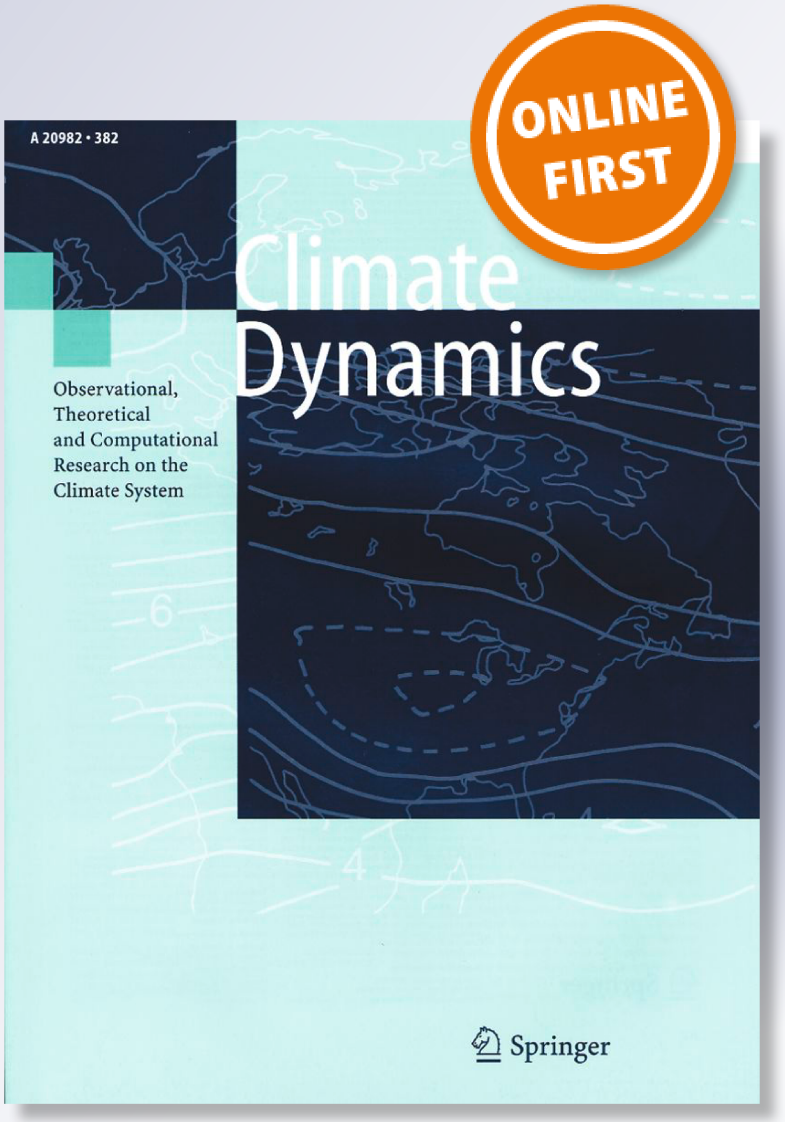

Springer

Clim Dyn
DOI 10.1007/s00382-017-3949-6

Modulation of the MJO intensity over the equatorial western Pacific by two types of El Niño

Lu Wang[1,2] · **Tim Li**[1,2] · **Lin Chen**[1,2] · **Swadhin K. Behera**[3] · **Tomoe Nasuno**[4]

Received: 6 May 2017 / Accepted: 1 October 2017

Abstract The modulation of the Madden–Julian Oscillation (MJO) intensity by eastern Pacific (EP) type and central Pacific (CP) type of El Niño was investigated using observed data during the period of 1979–2013. MJO intensity is weakened (strengthened) over the equatorial western Pacific from November to April during EP (CP) El Niño. The difference arises from distinctive tendencies of column-integrated moist static energy (MSE) anomaly in the region. A larger positive MSE tendency was found during the convection developing period in the CP MJO than the EP MJO. The tendency difference is mainly caused by three meridional moisture advection processes: the advection of the background moisture by the intraseasonal wind anomaly, the advection of intraseasonal moisture anomaly by the mean wind and the nonlinear eddy advection. The advections' differences are primarily caused by different intraseasonal perturbations and high-frequency activity whereas the background flow and moisture gradient are similar. The amplitudes in the intraseasonal suppressed convection anomaly over the central Pacific is critical in modulating the three meridional moisture advection processes. The influences on the central Pacific convection anomaly from seasonal mean moisture in two types of El Niños are discussed.

Keywords Madden–Julian oscillation · Western Pacific · El Niño · Moist static energy

1 Introduction

The Madden–Julian Oscillation (MJO) is the most prominent mode of intraseasonal variability in the tropics, characterized by an eastward propagating envelope of convective anomalies with a zonal wave number 1–3 spatial extent and 30–60-day time scale (Madden and Julian 1994). As it modulates deep convection in the tropics, the MJO has large impacts on a variety of weather and climate phenomena across different spatial and temporal scales (e.g., Zhang 2005; Wang et al. 2012). However, current state-of-art models have limited capacity in simulation of MJO and thus result in barrier of extended-range of forecast (Lin et al. 2006; Kim et al. 2011; Hung et al. 2013). Thus, it is of great interest by the society to understand the MJO because it could benefit extended-range of weather forecast.

An interannual variation has been seen in the MJO properties of intensity, periods, propagation and structures (e.g., Hendon et al. 1999; Kajikawa and Yasunari 2005; Lin and Li 2008a, b; Yang et al. 2008; Liu et al. 2016; Wang and Chen 2016), but the physical mechanisms for those are not well understood. It is of interest to figure out what controls the interannual variability of the MJO. Since El Niño-Southern Oscillation (ENSO) is the dominant mode of variability on interannual time scale, which could modulate global weather and climate (e.g., Chen et al. 2013, 2016a), the MJO-ENSO

✉ Tim Li
timli@hawaii.edu

1 Key Laboratory of Meteorological Disaster, Ministry of Education (KLME), Joint International Research Laboratory of Climate and Environmental Change (ILCEC), Collaborative Innovation Center on Forecast and Evaluation of Meteorological Disasters (CIC-FEMD), Nanjing University of Information Science and Technology, Nanjing, China

2 Department of Atmospheric Sciences, International Pacific Research Center, and School of Ocean and Earth Science and Technology, University of Hawaii, Honolulu HI, USA

3 Application Laboratory, JAMSTEC, Yokohama, Japan

4 Department of Seamless Environmental Prediction Research, JAMSTEC, Yokohama, Japan

Published online: 20 October 2017

connection has been widely investigated (Gutzler 1991; Fink and Speth 1997; Tang and Yu 2008). Statistically significant relationships between MJO and ENSO phase have been identified through observational analysis (Gutzler 1991), but the relationship between the MJO activity and ENSO index is of complex temporal and spatial characteristics (Hendon et al. 2007).

The simultaneous correlation between MJO convection variance and SST anomaly during the mature phase of ENSO (i.e., boreal winter) shows a maximum center over the equatorial Pacific region east of the dateline, where MJO convection usually dissipates. Fink and Speth (1997) suggested that the enhanced MJO variance close to the dateline in El Niño winter is due to the MJO convection that propagates farther eastward than normal-year, penetrating into the central Pacific. But the enhanced MJO variance as far east as the coast of South America is more closely tied to local intraseasonal oscillation in the atmosphere.

A statistically significant lagged correlation is also found between MJO and ENSO: the MJO is enhanced in spring–summer over the Indian Ocean and the western Pacific prior to the peak El Niño winter (Tang and Yu 2008; Chen et al. 2016b). Based on this, some studies argued that the MJO plays a role in triggering an El Niño (Kessler and Kleeman 2000; Bergman et al. 2001). For instance, the strengthened MJO could induce a stronger stochastic forcing like westerly wind burst (WWB) (Lau and Chan 1988), although the relevance of MJO to WWB remains an open question as the MJOs have a much larger spatial and temporal scales and evolve much less frequently than WWBs (Seiki and Takayabu 2007). Meanwhile, the MJO intensity may be modulated by El Niño (Moon et al. 2011, Hsu and Xiao 2017). The enhanced MJO prior to peak El Niño winter has been suggested to be related to large-scale background moisture and vertical sheared zonal wind anomalies associated with El Niño (Lin and Li 2008a, b; Deng et al. 2016; Liu et al. 2016).

The MJO–ENSO relationship was noted to vary with changes in ENSO's characteristic itself (e.g., Zhang and Gottschalck 2002; Tang and Yu 2008). Canonically, an El Niño event is characterized by anomalous SST warming over the eastern equatorial Pacific; since the 2000s, however, a new type of El Niño-featured by maximum SST anomalies over the central equatorial Pacific-has been reported. Various names are cited for this new flavor of El Niño, ranging from central Pacific El Niño, dateline El Niño, El Niño-Modoki, to warm pool El Niño (e.g., Ashok et al. 2007; Zhou et al. 2014; Feng and Li 2013). To facilitate the discussion, we employ the terminology of central Pacific El Niño (hereafter CP) to represent the new type of El Niño. Correspondingly, we use eastern Pacific (EP) El Niño to term the conventional El Niño. Therefore, it is better to separately investigate MJO–EP El Niño and MJO–CP El Niño relationships.

Comparing the MJO characteristics in the two types of El Niños, several contrasting aspects have been reported (Gushchina and Dewitte 2012; Feng et al. 2015; Chen et al. 2016b; Hsu and Xiao 2017). Over the equatorial Indian Ocean, where the MJO initiates and propagates eastward, the MJO convection activity during the developing and mature phase of El Niño (September–February) is stronger in CP El Niño than in EP El Niño (Hsu and Xiao 2017). The difference is due to the horizontal moisture advection related to both mean flows and local perturbations. Over the western Pacific, the MJO activity is enhanced during the predeveloping phase of EP El Niño, whereas no clear signals are seen during the predeveloping phase of CP El Niño (Chen et al. 2016b).

Recently, it is of interest to find that during the peak and decaying phases of El Niño, the MJO is weakened over the western Pacific in EP events while it is strengthened over the same region in CP events (see Fig. 5c in Gushchina and Dewitte 2012). But the mechanism behind this phenomenon is not clear. The current study tries to understand what cause the different MJO intensities over the western Pacific in the CP El Niño events and in the EP El Niño events.

The structure of this paper is as follows. The datasets and methods used in the study are described in Sect. 2. The characteristics of MJO intensities over the western Pacific in two types of El Niño are revealed in Sect. 3. Section 4 tries to identify the causes of differing MJO intensities by using a moist static energy (MSE) budget analysis. The influence of El Niño backgrounds is discussed in Sect. 5. The major findings are summarized in Sect. 6.

2 Data and method

2.1 Dataset

The datasets employed in this study include: (a) daily outgoing longwave radiation (OLR) data from NOAA (Liebmann and Smith 1996); (b) monthly SST data derived from the Hadley Center global sea ice and sea surface temperature data set (HadISST v1.1; Rayner et al. 2003); (c) daily atmospheric reanalysis data from ECMWF Interim Re-Analysis (ERA_I; Dee et al. 2011). The three-dimensional (3D) fields from ERA_I include zonal and meridional winds (u and v), pressure velocity (ω), temperature (T), specific humidity (q), and geopotential (ϕ) at 19 levels from 1000 to 100 hPa with a 50-hPa interval. The surface fields contain sensible heat flux, latent heat flux, longwave and shortwave fluxes at the bottom and top of the atmosphere. The analysis period for all the data spans from 1979 to 2013 and all datasets are archived on a grid resolution of 2.5°.

2.2 Methods

Following Chen et al. (2016b), temporal evolutions of any given field corresponding to two types of El Niño could be easily obtained by using a partial regression method, that is, regression onto a pair of El Niño indices in the form of $\hat{X} = a_0 + b_1 N_{EP} + b_2 N_{CP}$. Here, $\hat{X}$ represents any given monthly time series; N_{EP} and N_{CP} denote a pair of standardized El Niño indices; b_1 (b_2) represents the contribution from EP (CP) El Niño. We define *Niño*-3 region (5°S–5°N, 150°W–90°W) averaged monthly SST anomalies as N_{EP} and El Niño Modoki index (see definition in Ashok et al. 2007) as N_{CP}. This partial regression method could partly eliminate the simultaneous influence from both types of El Niños. Student's t-test is applied to the partial regression coefficients.

A variety of indexes have been proposed to isolate the MJO signal, and each of them has its own strengths and weaknesses (e.g., Wheeler and Kiladis 1999; Wheeler and Hendon 2004). In this study, we mainly use the 30–90 day bandpass-filtered (Duchon 1979) daily OLR with a removal of climatological annual cycle to represent the MJO convection, and therefore measure the MJO amplitude by the standard deviation (SD) of the time-filtered OLR anomaly. This method has been employed by many previous studies (e.g., Chen et al. 2016b; Wang et al. 2017). In addition, we also employ some other MJO definitions to estimate the dependence of the results on the choice of MJO indexes. One method is to filter daily OLR in both frequency and zonal wavenumber space (i.e., 30–90 day, zonal wavenumber 1–5) with the filter proposed by Wheeler and Kiladis (1999). The other is the real-time multivariate (RMM) MJO index (Wheeler and Hendon 2004), which is obtained by first two principal components (PCs) of OLR, 850-hPa zonal wind, and 200-hPa zonal wind averaged 15°S–15°N.

An intraseasonal MSE budget analysis is used to identify what causes the difference in MJO amplitude between the EP and CP El Niños. MSE (m) is defined as $m = c_p T + gz + L_v q$, where T is temperature, z is height, q is specific humidity, c_p is the specific heat at constant pressure (1004 J K^{-1} kg^{-1}), g is the gravitational acceleration (9.8 m s^{-2}) and L_v is the latent heat of vaporization (2.5×10^6 J kg^{-1}). The intraseasonal column-integrated MSE budget can be written as follows (Neelin and Held 1987)

$$\langle \partial_t m \rangle' = \left\langle -\vec{V}_3 \cdot \nabla_3 m \right\rangle' + Q_t' + Q_r', \tag{1}$$

where angle brackets represent a mass-weighted vertical integral from the surface to 100 hPa level, p is pressure and $\vec{V}_3$ is three-dimensional wind vectors. The lhs term represents MSE tendency; $-\vec{V}_3 \cdot \nabla_3 m$ denotes three-dimensional advection of m; Q_t represents sum of surface latent and sensible heat fluxes and Q_r is net column-integrated shortwave and longwave heating rates. Here Q_r is estimated as the difference between the surface and top of atmosphere fluxes. A prime represents perturbations on intraseasonal time scale, which are obtained by regression onto an intraseasonal OLR index.

3 Observed MJO characteristics during the two types of El Niños

Figure 1 shows the evolution of 10°S–10°N averaged SST (contour) over the central and eastern Pacific as well

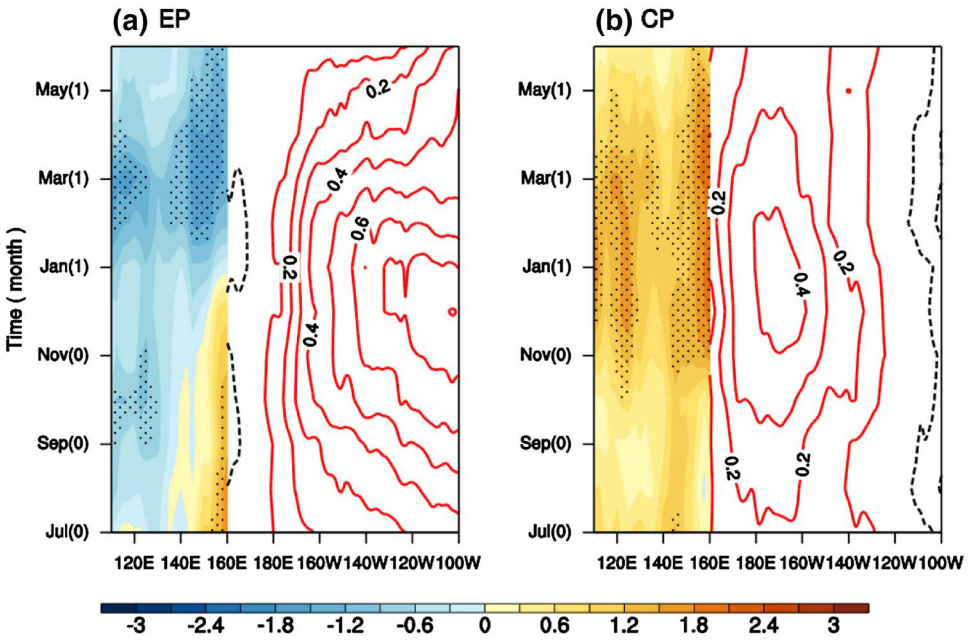

Fig. 1 Evolution of monthly mean SST anomalies (contour, K) and monthly MJO intensity (color, W m^{-2}) averaged over 10°S–10°N relative to **a** EP and **b** CP El Niño. The evolution of MJO intensity and SST are obtained by partially regressing them onto the EP and CP El Niño indices averaged from December to February. Monthly MJO intensity is estimated as the standard deviation of 30–90 day filtered OLR anomalies with a 3-month moving window. Results passing the significant test at 90% confidence level are stippled for MJO intensity anomalies. Here 0 (1) denotes El Niño developing (subsequent) year

as MJO intensity (shaded) over the western Pacific with time and longitude corresponding to the two types of El Niños, respectively. This is obtained by partial regression of monthly SST anomaly and monthly MJO intensity onto the indices of two types of El Niños averaged over December-February. 0 (1) represents El Niño onset (subsequent) year. In EP El Niño, positive SST anomalies are confined to the east of the dateline with a peak east of 120°W in Dec(0). In CP El Niño, positive SST anomalies with smaller intensity than in EP El Niño are confined over the central Pacific with a center at 170°W. The evolutions of SST anomalies associated with two types of El Niños agree with the findings documented in previous studies (e.g., Ashok et al. 2007), so it gives us the confidence to use this partial regression method to reveal the evolution features of MJO intensity.

The monthly MJO intensity for regression is calculated by SD of 30–90 day filtered OLR anomaly with a 3-month moving window following Hendon et al. (2007). It is interesting to find that the MJO intensity tends to be suppressed over the western Pacific in the EP El Niño but enhanced in the CP El Niño. Furthermore, this contrasting feature is most prominent during the mature and decaying phases of El Niño [i.e., Nov(0) to Apr(1)]. Such a result would not change if we use another pair of El Niño indices defined by Ren and Jin (2011) or if we calculate the monthly MJO intensity by SD of time–space filtered OLR anomaly (figures not shown).

Are the distinctive MJO intensities over the equatorial western Pacific between the two types of El Niños significant? To obtain more evidence, we then calculate MJO intensities during November–April of each year (SD of 30–90 day filtered OLR anomalies) and do composite for the EP El Niño events and the CP El Niño events in 1979–2013 respectively. Four EP El Niño years (1982, 1986, 1991, 1997) and four CP El Niño years (1994, 2002, 2004, 2009) are selected during 1979–2013. The major EP and CP El Niño years are identified primarily following McPhaden et al. (2011) and Hsu and Xiao (2017), except for one less year in CP El Niño group. Xiang et al. (2013) and Chung and Li (2013) had a detailed discussion on why the four CP events are classified as "pure" CP El Niño events and how they differ from other mixed events. It is worth mentioning that the classification of a few El Niño events is debatable; for instance, the El Niño 1986–1987 became as an EP event but continued as a CP type and the El Niño 2006–2007 is considered as a CP event in some studies (e.g., Takahashi et al. 2011). Figure 2 displays horizontal maps of difference in MJO intensity between the EP and the CP El Niño events (CP minus EP). It is clearly seen that the CP El Niño displays significant stronger MJO intensity than the EP El Niño over the western Pacific (120°–150°E). This result remains the same when we do a parallel calculation by using SD of the time–space filtered OLR anomlay (figure not shown). Therefore, we will focus on the box of 10°S–10°N, 120°–150°E over the western Pacific in the following to examine how the two types of El Niño exert different influences on MJO activities based on an MSE budget analysis.

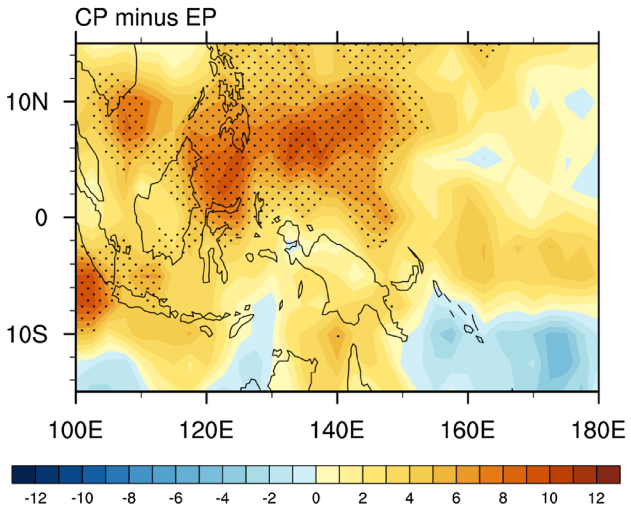

Fig. 2 Difference in boreal-winter MJO intensity (i.e., standard deviation of 30–90 day filtered OLR during November–April, units: W m^{-2}) between the EP El Niño events and the CP El Niño (CP minus EP). Results passing the significant test at 90% confidence level are stippled

4 Moist static energy budget and mechanism for MJO intensity difference

In the paradigm that describes the MJO as a moisture mode (e.g., Raymond and Fuchs 2009; Sobel and Maloney 2013), the MJO's lifecycle depends fundamentally on variations in atmospheric water vapor. Under the weak temperature gradient condition (Sobel et al. 2001), column-integrated MSE is also primarily regulated by column moisture. Therefore, the evolution of column MSE (or moisture) could well represent the evolution of an MJO envelop, and it is reasonable to conduct MSE budget analysis in a composite MJO lifecycle to understand the primary causes for its evolution.

Prior to performing MSE budget analysis, we first compare Hovmöller patterns of convection anomalies and column-integrated MSE anomalies associated with MJO in EP El Niño and MJO in CP El Niño (hereafter EP MJO/CP MJO), respectively. This is obtained by lag-regression of unfiltered daily OLR and MSE fields onto a western Pacific MJO index that is represented by 30–90 day filtered OLR anomalies averaged over 10°S–10°N, 120°–150°E during November–April. Note that the sign of the OLR index has been reversed prior to regression, such that a negative (positive) value in regressed OLR anomaly indicates enhanced (suppressed) convection. In both cases, the propagation and amplitude evolutions of positive anomaly in

column-integrated MSE agree very well with the enhanced convection, except that it has several days leading of the convection due to a lead of moisture anomaly in lower troposphere and planetary boundary layer (PBL) (Maloney 2009). For the EP MJO (Fig. 3a), enhanced convection reaches its maximum of around 9 W m^{-2} at day 0 over the western Pacific. By contrast, the CP MJO convection reaches its maximum amplitude at day 0 of more than 12 W m^{-2}. We did parallel calculations by using time–space filtered OLR or composite OLR anomaly based on RMM index and obtained similar results (figures not shown).

Then the temporal evolutions of $<m'>$ averaged over the base region of western Pacific (10°S–10°N, 120–150°E) from day −30 to day +30 associated with the EP MJO and the CP MJO are displayed in Fig. 4a. Note that the MJO convection reaches its peak at day 0, and negative (positive) lags denote the developing (decaying) phase of MJO convection. The CP MJO has a peak value in $<m'>$ of 5×10^6 J m^{-2} near day 0, which is apparently larger than that in EP MJO (less than 4×10^6 J m^{-2}), although their peak values show small shifts in lagged time. As is known, a peak amplitude is due to both growth rate and time-scale for growth. Comparing the temporal evolutions of $<m'>$ in Fig. 4a, it is found that the larger peak value in the CP MJO is primarily a result from a greater developing rate during day −20 to day −5; the positive $<\partial m'/\partial t>$ in CP MJO is around two times as large as that in EP MJO (see Fig. 4b). Therefore, we mainly focus on the MSE tendency difference over day −20 to day −5 between the two groups of MJOs in the following.

Figure 5 displays the difference in each MSE budget term between the CP MJO and the EP MJO during the positive

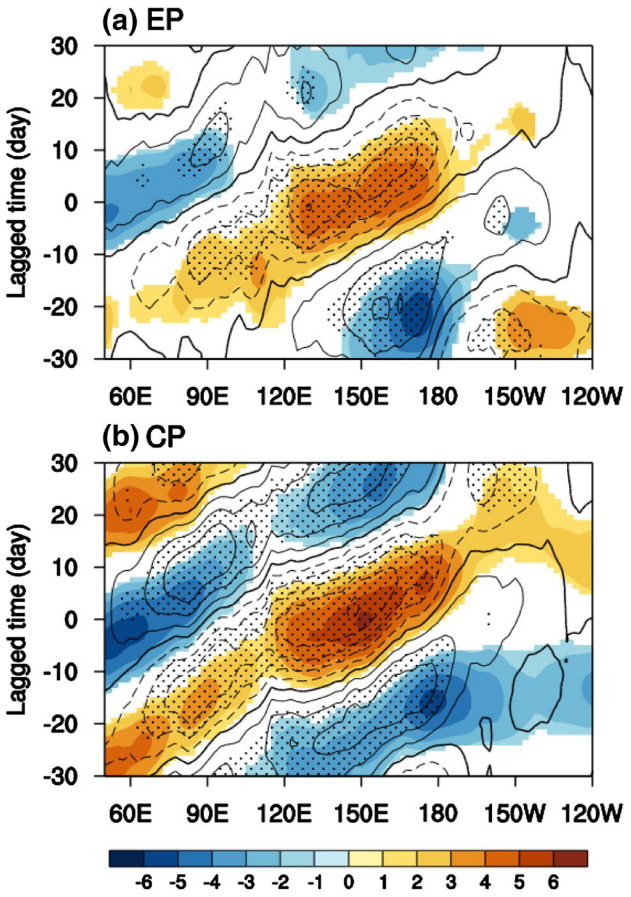

Fig. 3 Hovmöller diagram of OLR anomaly (contour, W m^{-2}) and vertical-integrated (surface to 100 hPa) MSE anomaly (shaded, $\times 10^6$ J m^{-2}) for **a** EP MJO and **b** CP MJO. They are obtained by lag regression onto the western Pacific MJO index over 10°S–10°N, 120°–150°E during November–April. Dashed contours are for negative values (enhanced convection), and zero contours are bold. Results passing the significant test at 90% confidence level are stippled for anomalous OLR and presented for anomalous vertical-integrated MSE

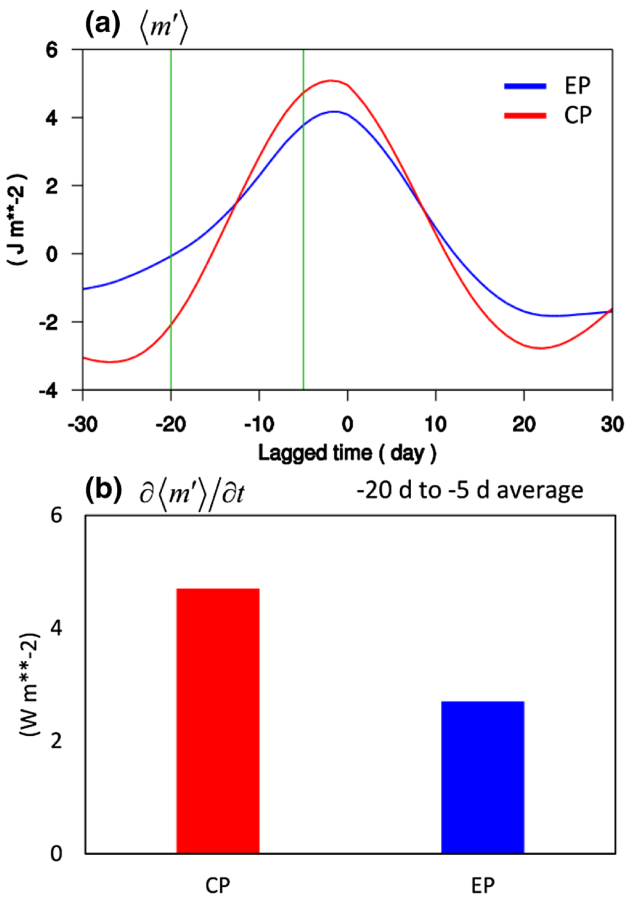

Fig. 4 **a** Temporal evolution of column-integrated (surface to 100 hPa) MSE anomaly ($\times 10^6$ J m^{-2}) over the key region 10°S–10°N, 120°–150°E as a function of lagged time for EP MJO (blue) and CP MJO (red). Here day 0 denote the time when the MJO convection reaches its peak over the key region and negative (positive) lags denote the time prior to (after) the convection peak. The vertical lines in **a** denote common positive tendency period of MSE anomaly (i.e., day −20 to day −5). **b** Tendency of column-integrated MSE anomaly (W m^{-2}) averaged from day −20 to day −5 for EP MJO (blue bar) and CP MJO (red bar)

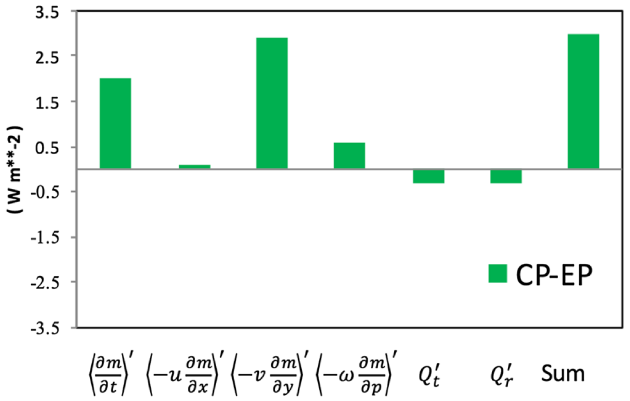

Fig. 5 Difference in MSE budget terms (W m^{-2}) between the CP MJO and the EP MJO (CP minus EP) averaged over the positive MSE tendency period (day −20 to day −5) in the key region 10°S–10°N, 120°–150°E. Each term is vertically integrated from surface to 100 hPa. Bars from left to right represent column-integrated MSE tendency, column-integrated zonal MSE advection, column-integrated meridional MSE advection, column-integrated vertical MSE advection, surface heat flux (Q_t), radiative heating (Q_r) and the sum of budget terms

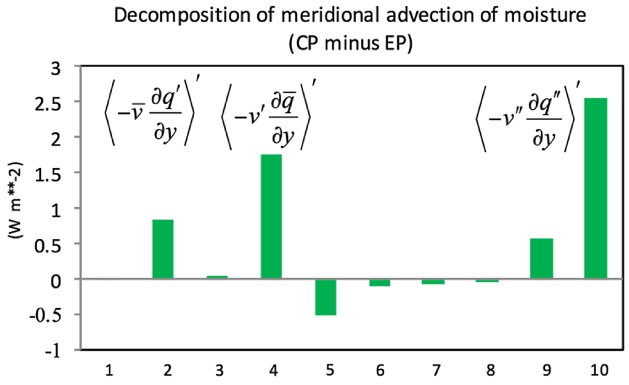

Fig. 6 Difference in meridional moisture advection term between the CP MJO and the EP MJO (CP minus EP) averaged over the positive MSE tendency period (day −20 to day −5) in the key region 10°S–10°N, 120°–150°E. The terms from left to right are: (1) $<-\bar{v}\partial\bar{q}/\partial y>'$, (2) $<-\bar{v}\partial q'/\partial y>'$, (3) $<-\bar{v}\partial q''/\partial y>'$, (4) $<-v'\partial\bar{q}/\partial y>'$, (5) $<-v'\partial q'/\partial y>'$, (6) $<-v'\partial q''/\partial y>'$, (7) $<-v''\partial\bar{q}/\partial y>'$, (8) $<-v''\partial q'/\partial y>'$, (9) $<-v''\partial q''/\partial y>'$, (10) sum of terms 1–9. Each term is vertically integrated from surface to 100 hPa and is multiplied by L_v, so it shows comparable units to column-integrated MSE tendency (W m^{-2})

tendency period (averages from day −20 to day −5). The positive shift in $\langle\partial m/\partial t\rangle'$ in CP MJO compared to the EP MJO is primarily due to the positive shift in meridional MSE advection ($\langle -v\partial m/\partial y\rangle'$), while the other terms are negligible. The MSE budget results are nearly balanced, although some residuals are necessarily introduced because of the analysis increment used in producing reanalysis data and the neglect of rapid (<1 day) eddy transport in off-line calculation of advection terms relative to the model's internally calculated advection (Kiranmayi and Maloney 2011).

Since meridional MSE advection is almost entirely due to its moisture component $\langle -v\partial(L_v q)/\partial y\rangle'$ (figure not shown), we only analyze the meridional moisture advection term $\langle -v\partial q/\partial y\rangle'$ in the following. Both meridional wind (v) and moisture (q) are partitioned into a low-frequency background component (>90 days, indicated by an overbar), an intraseasonal component (indicated by a prime) and a higher-frequency component (<20 days, indicated by a double-prime) (i.e., $q=\bar{q}+q'+q''$,$v=\bar{v}+v'+v''$), so that the product of v and $\partial q/\partial y$ yields nine terms. The difference in each component of $\langle -v\partial q/\partial y\rangle'$ between the CP MJO and the EP MJO is displayed in Fig. 6. It is clearly shown that the more positive MSE tendency in the CP MJO than in the EP MJO is mainly caused by three terms: (1) advection of background moisture by intraseasonal meridional wind anomaly ($-v'\partial\bar{q}/\partial y$), (2) advection of intraseasonal moisture anomaly by background meridional wind ($-\bar{v}\partial q'/\partial y$) and (3) meridional moisture advection due to nonlinear eddy advection ($-v''\partial q''/\partial y$).

Given that both the background state and the perturbation components (intraseasonal or high-frequency) are distinct between the CP and the EP events, one may wonder to what extent the background state difference and the perturbation difference contribute to the differences in the three advection terms. Prior to separating these terms one by one in the following subsections, we check the vertical profiles of the three advection terms and find they are very small above 400 hPa level (figure not shown) since moisture is lacked in upper troposphere. Examination of the vertical structure of the intraseasonal wind anomalies shows that the transition zone of wind inversion is near 400 hPa (figure not shown). This suggests that we may concentrate our analysis of each term on the part that vertically averaged from surface to 400 hPa.

4.1 Advection of background moisture by intraseasonal meridional wind anomaly

Figure 7 displays meridional structures of seasonal mean moisture averaged from surface to 400 hPa over the western Pacific region composited for the CP El Niño and the EP El Niño. In both cases, the seasonal mean moisture reaches the maximum at 2.5°S and decreases with latitude toward poles. Thus, we may separate the key region (i.e., 10°S–10°N) into a middle region (ranging from 5°S to 0°S) where $\partial\bar{q}/\partial y$ is near zero, a northern region (ranging from 0° to 10°N) where $\partial\bar{q}/\partial y$ is negative, and a southern region (ranging from 10°S to 5°S) where $\partial\bar{q}/\partial y$ is positive. Then the question becomes as which sub-region does the difference in $-v'\partial\bar{q}/\partial y$ between the CP MJO and the EP MJO arise from, the northern region or the southern region?

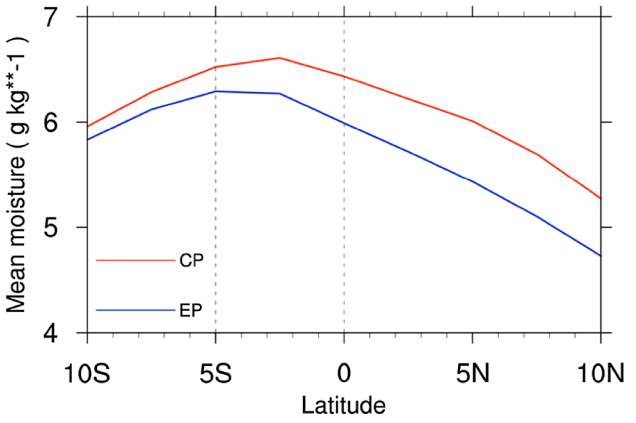

Fig. 7 Meridional profiles of seasonal mean (November–April) specific humidity ($\bar{q}$, g kg^{-1}) averaged over surface to 400 hPa in the key region (120°–150°E) composite for the CP El Niño (red) and the EP El Niño (blue). Dashed lines separate the region of interest into three sub-regions with different meridional gradients of mean moisture

Figure 8a presents the northern-region averaged and the southern-region averaged $-v'\partial\bar{q}/\partial y$ during the MSE positive tendency period (averages from day −20 to day −5) for the CP MJO and EP MJO respectively. This term is positive in both cases and in both regions, and the more positive value in the CP MJO arises from the northern region component, which is about twice as large as that in the EP MJO. Since the meridional gradients of seasonal mean moisture between the CP and the EP MJOs are very similar in the northern region (Fig. 8b), the difference is attributed to stronger northward wind anomaly in the CP MJO than in the EP MJO (Fig. 8c).

Then why the northward wind anomaly is observed in the northern region in both MJO cases and why it is weaker in EP MJO than in CP MJO? Figure 9 displays horizontal distributions of OLR and 1000–400 hPa vertically averaged wind fields lag-regressed onto the western Pacific MJO index (averages from day −20 to day −5) for the CP MJO and the EP MJO respectively. In both cases, a zonal dipole of convection anomaly is observed, which is characterized by an enhanced convection anomaly (i.e., negative OLR anomaly) over the eastern Indian Ocean and a suppressed convection anomaly (i.e., positive OLR anomaly) over the central Pacific Ocean (150°E to the dateline). The anomalous convections induce anomalous atmospheric heating, which then drive Gill response in atmospheric circulations (Gill 1980). Therefore, over the western Pacific region (black box), the easterly wind anomalies at the equator are due to a Kelvin wave response to the positive heating over the eastern Indian Ocean, meanwhile the poleward meridional wind anomalies off the equator are due to a Rossby wave response to the negative heating over the central Pacific Ocean. Such a coupled dipole convection and circulation pattern was also revealed

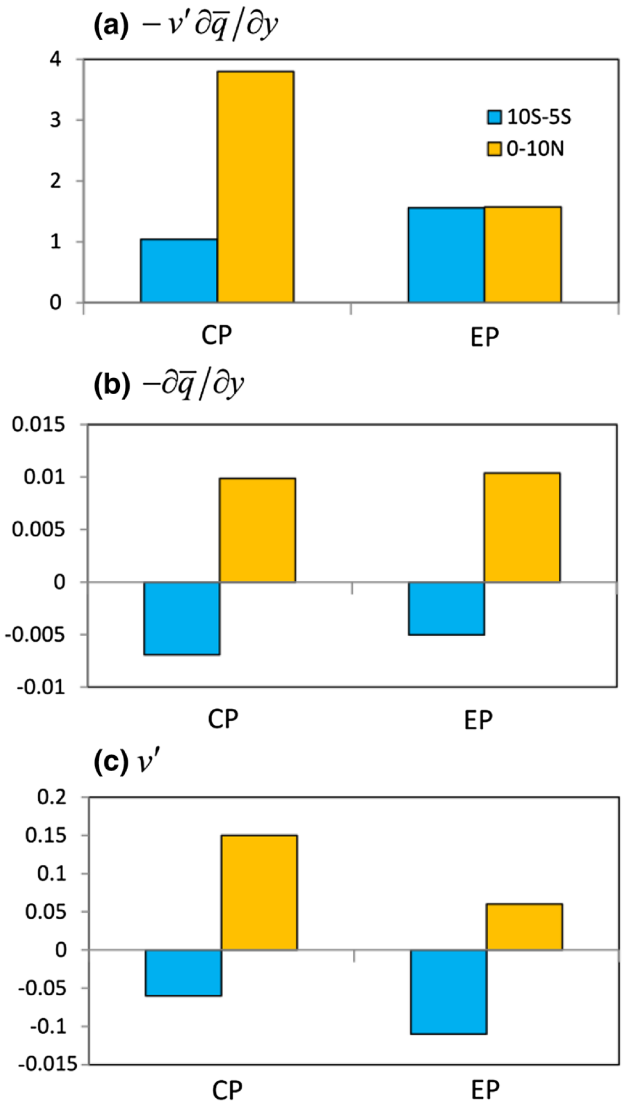

Fig. 8 **a** Advection of background moisture by intraseasonal meridional wind anomaly ($-v'\partial\bar{q}/\partial y$, units: 10^{-9} s^{-1}) averaged over the positive MSE tendency period (day −20 to day −5) for the CP MJO and the EP MJO. **b** Meridional gradient of seasonal mean (November–April) moisture ($-\partial\bar{q}/\partial y$, units: 10^{-6} m^{-1}) composite for CP El Niño and EP El Niño. **c** Intraseasonal meridional wind anomaly (v', units: m s^{-1}) over the positive MSE tendency period (day −20 to day −5) for the CP MJO and the EP MJO. Each term is vertically averaged over surface to 400 hPa. Orange (blue) bars represent the northern region 0°–10°N, 120°–150°E average (southern region 10°S–5°S, 120°–150°E average)

by Kim et al. (2014) and Wang et al. (2017). Comparing the two MJO cases, the central-Pacific suppressed convection anomaly (and the related negative atmospheric heating anomaly) is weaker to the north of the equator in the EP MJO than that in the CP MJO. Therefore, the northern-hemisphere northward wind anomaly over the western Pacific is suppressed in the EP MJO compared to that in the CP MJO.

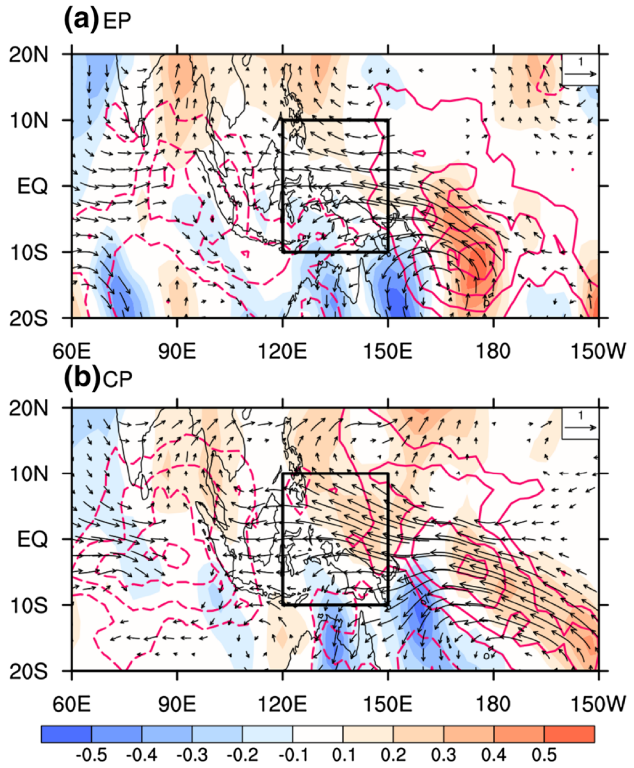

Fig. 9 Intraseasonal anomalies in OLR (W m^{-2}, contour, interval 3) and wind fields vertically averaged over surface to 400 hPa (vector, m s^{-1}) during the positive MSE tendency period (day −20 to day −5) for **a** the EP MJO and **b** the CP MJO. Vectors are present where wind speeds are greater than 0.1 m s^{-1} and the meridional wind component is shaded. Dashed contours are for negative values and zero contours are omitted. The boxes mark the key region 10°S–10°N, 120°–150°E

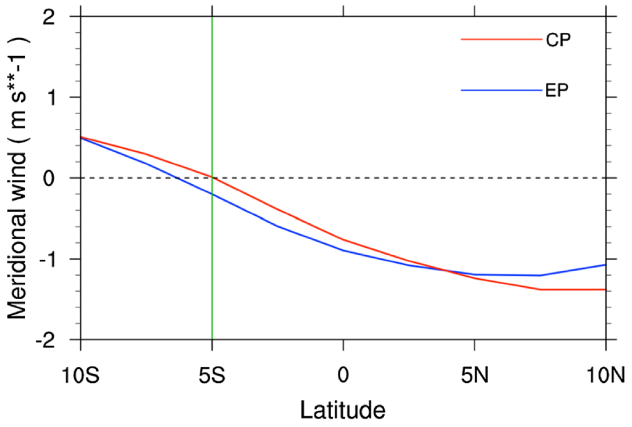

Fig. 10 Meridional profiles of seasonal mean (November–April) meridional wind ($\bar{v}$, m s^{-1}) averaged over surface to 400 hPa in the key region (120°–150°E) composite for the CP El Niño (red) and the EP El Niño (blue)

4.2 Advection of intraseasonal moisture anomaly by background meridional wind

We first examine the meridional structures of seasonal mean meridional wind averaged over surface to 400 hPa in the western Pacific region (Fig. 10). They are found to be very similar in the two types of El Niño years, so we separate the key region (10°S–10°N) into a northern region (5°S–10°N) where the wind is southward and a southern region (10°S–5°S) where the wind is northward. Then the issue becomes as which sub-region does the difference in $-\bar{v}\partial q'/\partial y$ between the CP MJO and the EP MJO arise from, the northern region or the southern region?

Figure 11a presents the northern-region averaged and the southern-region averaged $-\bar{v}\partial q'/\partial y$ during the MSE positive tendency period (averages from day −20 to day −5) for the CP MJO and EP MJO respectively. This term is negative in the EP MJO and is near zero in the CP MJO. Its positive shift in the CP MJO is primarily due to the northern region component. Since the amplitudes of mean southward wind are very similar in the EP and the CP El Niño years (Fig. 11b), the difference is resulted from meridional gradient of anomalous moisture between the CP MJO and EP MJO. As one can see, $\partial q'/\partial y$ over the northern region in the EP MJO case is apparently positive while it is near zero in the CP MJO.

Figure 12 presents intraseasonal moisture anomaly in the positive MSE tendency period (day −20 to day −5) for the CP MJO and the EP MJO overlaid by seasonal mean wind fields composited for the CP El Niño year and the EP El Niño year; they are all vertically averaged over surface to 400 hPa. In the EP MJO, the positive center of moisture anomaly over the western Pacific is confined to the south of the equator so the meridional gradient of moisture anomaly ($\partial q'/\partial y$) is largely negative in the northern region (5°S–10°N). Given the seasonal mean wind is southward in the northern region, the advection term of $-\bar{v}\partial q'/\partial y$ is largely negative. By contrast, in the CP MJO, the maximum moisture anomaly centers are on both sides of the equator. Therefore, the meridional gradient of moisture anomaly over the western Pacific is near zero, and so does the advection term of $-\bar{v}\partial q'/\partial y$.

What causes the different meridional distributions of the intraseasonal moisture anomalies over the western Pacific? Fig. 13a, b examine the evolutions of the 120°–150°E averaged moisture anomalies from day −25 to day −5 with an average over 5 days for the EP MJO and the CP MJO, respectively. In the EP MJO, the maximum center in moisture anomaly to the south of the equator can be found as early as day −25 and then the pattern has little change except its amplitude (Fig. 13a). In the CP MJO, the maximum centers in the moisture anomaly on both sides of the equator are formed after day −15 (Fig. 13b). We examine the horizontal distributions of the moisture anomaly and the advection of mean moisture by MJO wind anomalies averaged over day

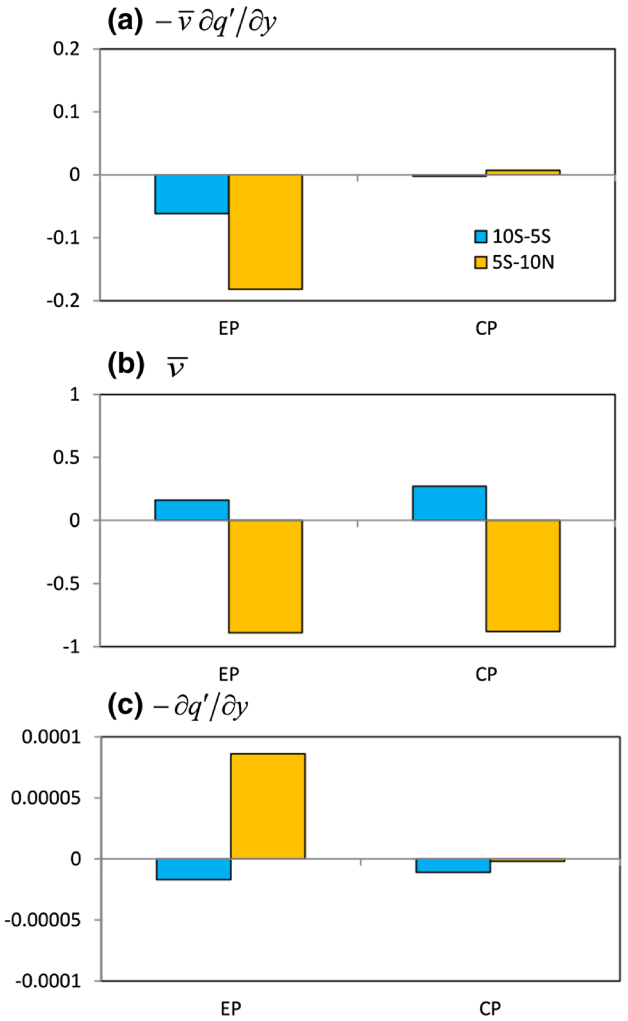

Fig. 11 **a** Advection of intraseasonal moisture anomaly by background meridional wind ($-\bar{v}\partial q'/\partial y$, units: 10^{-9} s^{-1}) averaged over the positive MSE tendency period (day −20 to day −5) for the CP MJO and the EP MJO. **b** Seasonal mean (November–April) of meridional wind ($\bar{v}$, units: m s^{-1}) composite for CP El Niño and EP El Niño. **c** Meridional gradient of intraseasonal moisture anomaly ($-\partial q'/\partial y$, units: 10^{-6} m^{-1}) over the positive MSE tendency period (day −20 to day −5) for the CP MJO and the EP MJO. Each term is vertically averaged over surface to 400 hPa. Orange (blue) bars represent the northern region 5°S–10°N, 120°–150°E average (southern region 10°S–5°S, 120°–150°E average)

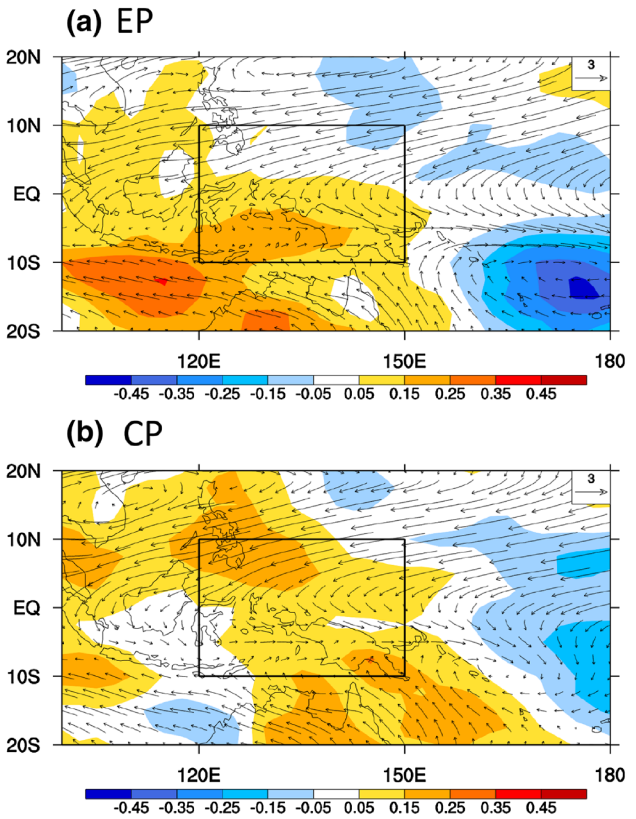

Fig. 12 **a** Horizontal distribution of intraseasonal moisture anomalies (shaded, g kg^{-1}) over the positive MSE tendency period (day −20 to day −5) of EP MJO and seasonal mean (November–April) wind fields (vectors, m s^{-1}) composite for EP El Niño events. **b** Same as in **a**, except for CP El Niño events. Both moisture anomalies and wind fields are vertically averaged over surface to 400 hPa

−20 to day −5 for the CP MJO (Fig. 13c), and find that their patterns are very similar. This suggests that the distributions of the moisture anomalies over the western Pacific in the CP MJO are possibly due to the advection term. However, what causes the initial moisture profile in the EP MJO is not clear.

4.3 Nonlinear eddy advection

Maloney (2009) pointed out that high-frequency disturbances act to mix humidity between the tropics and the extratropics, so suppression of them could generate anomalous moistening in atmosphere while strengthening of them generate anomalous drying. Figure 14 compares the nonlinear high-frequency advection term and the strength of high-frequency activities during the positive MSE tendency period (averages from day −20 to day −5) vertically averaged from surface to 400 hPa for the EP MJO and the CP MJO. The latter is obtained by lag-regression of daily kinetic energy, which is calculated by high-pass filtered wind anomaly ($u''^2 + v''^2$), onto the western Pacific MJO index and then take an average from day −20 to day −5. Negative anomaly in it indicates suppressed high-frequency activities on intraseasonal time scale. In the CP MJO, the advection term is strongly positive while the high-frequency activity is strongly suppressed; in the EP MJO, the advection term is weakly positive while the high-frequency activity is weakly suppressed. This relationship agrees well with the theory proposed by Maloney (2009). Therefore, the more positive non-linear advection term in the CP MJO relative to the EP MJO is related to the more suppressed high-frequency activities on intraseasonal time scale over the western Pacific.

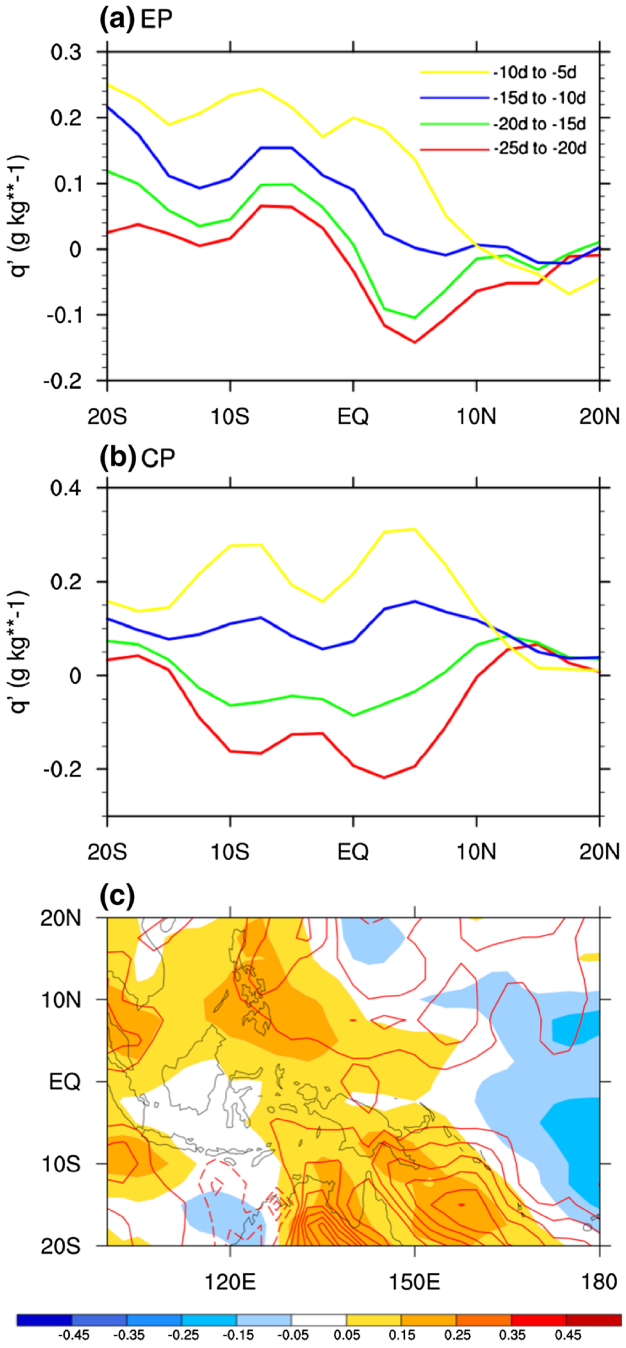

Fig. 13 **a** Meridional distributions of 120°E–150°E averaged intraseasonal moisture anomaly (q′, g kg^{-1}) for the EP MJO. Different colors represent 5-day average results over different periods (marked in upper right corner). The moisture anomalies are vertically averaged over surface to 400 hPa. **b** same as in **a**, except for the CP MJO. **c** Horizontal distribution of intraseasonal moisture anomaly (shaded, g kg^{-1}) and advection of mean moisture by intraseasonal wind anomalies (i.e., $\left(-v'\partial\,\bar{q}\,/\partial y\right)'$, contour, units: 10^{-9} s^{-1}) over the positive MSE tendency period (day −20 to day −5) of CP MJO. Dashed contours are for negative values and zero contours are omitted

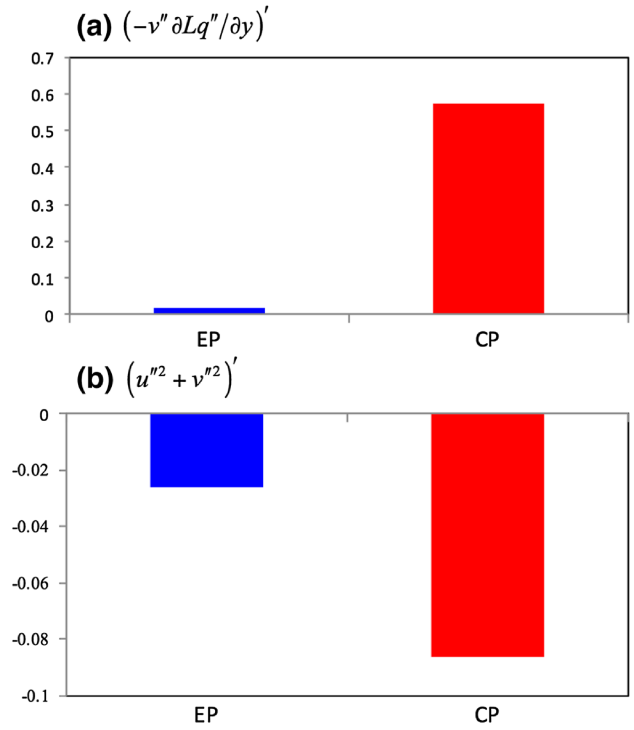

Fig. 14 **a** Meridional moisture advection due to nonlinear eddy advection over the positive MSE tendency period (day −20 to day −5) of the CP MJO (red) and the EP MJO (blue). **b** same as in **a**, except for kinetic energy calculated by high-frequency eddies ($(u''^2+v''^2)'$). All results are vertically averaged over surface to 400 hPa

Figure 15a, b display the horizontal distributions of the vertically averaged (surface to 400 hPa) intraseasonal eddy kinetic energy anomalies averaged over day −20 to day −5 for the EP MJO and the CP MJO, overlaid by the corresponding intraseasonal OLR anomaly (same as in Fig. 9). As one can see, the region of the negative eddy activity anomaly is mainly confined to the south of the equator in the EP MJO, while it has a northwest-southeast tilted pattern and is across the equator in the CP MJO. The different horizontal patterns of the eddy activity anomaly, therefore, result in that the eddy activity is more suppressed over the key box, which is at the equator, in the CP MJO compared to the EP MJO. Comparing the horizontal patterns of the eddy activity anomaly and that of the OLR anomaly, we find that the suppressed eddy activity follows that of the positive OLR anomaly (suppressed convection anomaly) very well. We further calculate the pattern correlation coefficients between the eddy kinetic energy anomaly and the OLR anomaly over the region 20°S–20°N, 100°–180°E at each lagged day from day −25 to day −5 for the CP MJO and EP MJO (Fig. 15c). Both cases show significant negative correlation coefficients. The good pattern relationship suggests that the suppressed

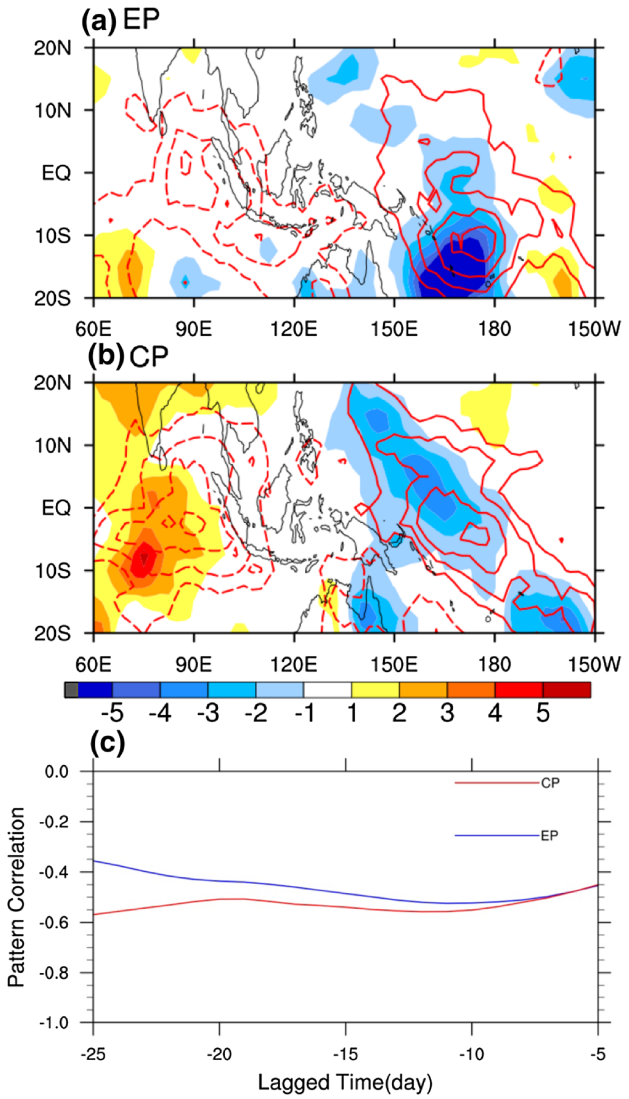

Fig. 15 **a** Intraseasonal anomalies in OLR (contour, W m^{-2}) and kinetic energy (shaded, m^2 s^{-2}) calculated by high-frequency eddies $\left(\left(u'^2 + v'^2\right)'\right)$ vertically averaged over surface to 400 hPa and averaged over the positive MSE tendency period (day −20 to day −5) for the EP MJO. Dashed contours are for negative values and zero contours are omitted. **b** Same as in **a**, except for the CP MJO. **c** Pattern correlation coefficients between the OLR anomaly and the kinetic energy anomaly over 20°S–20°N, 100°–180°E at each day from day −25 to day −5. The 95% confidence interval for the correlation coefficient is 0.1

eddy activity is modulated by the suppressed intraseasonal convection anomaly.

5 Discussion

The above section has revealed that the magnitude of the central-Pacific (150°E to the dateline) suppressed intraseasonal convection anomaly during day −20 to day −5 between the CP MJO and the EP MJO is critical in modulating the three meridional moisture advection terms; it is apparently weaker north of the equator in the EP MJO compared to the CP MJO (Fig. 9). In this section, we will discuss how the two types of El Niño influence the intraseasonal suppressed convection anomaly.

Figure 16 a, b display November–April averaged 850-hPa moisture and 500-hPa pressure velocity composite for the EP El Niño and the CP El Niño, in which the climatological average has been subtracted. In general, a dipole structure of moisture anomalies can be seen in both the EP El Niño and the CP El Niño, that is a negative anomaly to the west and a positive anomaly to the east. However, their magnitudes are apparently different, especially over the northern hemisphere. In the EP El Niño, the negative moisture anomaly is strong and covers a broad region from the Maritime Continent to the dateline. In comparison, the negative moisture anomaly in the CP El Niño is weak and only confined to the Maritime Continent. It suggests that over the northern central Pacific the mean moisture is much less in the EP El Niño than in the CP El Niño. Thus, even given the same MJO flows, the resulted intraseasonal convection anomaly would be weaker in the EP MJO than in the CP MJO. The less mean moisture in the EP El Niño is due to stronger descending motion over the middle troposphere.

Figure 16c, d further compares the winter mean SST anomaly in the EP El Niño and the CP El Niño. A significant difference can be found in the negative SST anomaly; the EP El Niño has a much stronger cold SST anomaly, especially to the north of the equator. Since cold surface is in favor of atmospheric descending motion, the different magnitudes of the negative SST anomaly between the two types of El Nino may explain the different strengths in descending motion anomaly and thus the mean moisture.

6 Summary

In this study, we examined different influences of two types of El Niño on MJO intensities over the equatorial western Pacific region. The El Niño events during the period of 1979–2013 are classified into EP El Niño and CP El Niño types based on previous studies. Both partial regression and composite analysis show that during the peak and decaying phase of El Niño (November–April), the EP events are associated with weakened MJO over the equatorial western Pacific whereas the CP events are associated with strengthened MJO.

An analysis of column-integrated MSE budget was performed for EP MJO and CP MJO respectively. The ultimately bifurcated peak magnitudes of MJO convection arises from different MSE tendencies over the convection developing period (day −20 to day −5). The MSE tendency

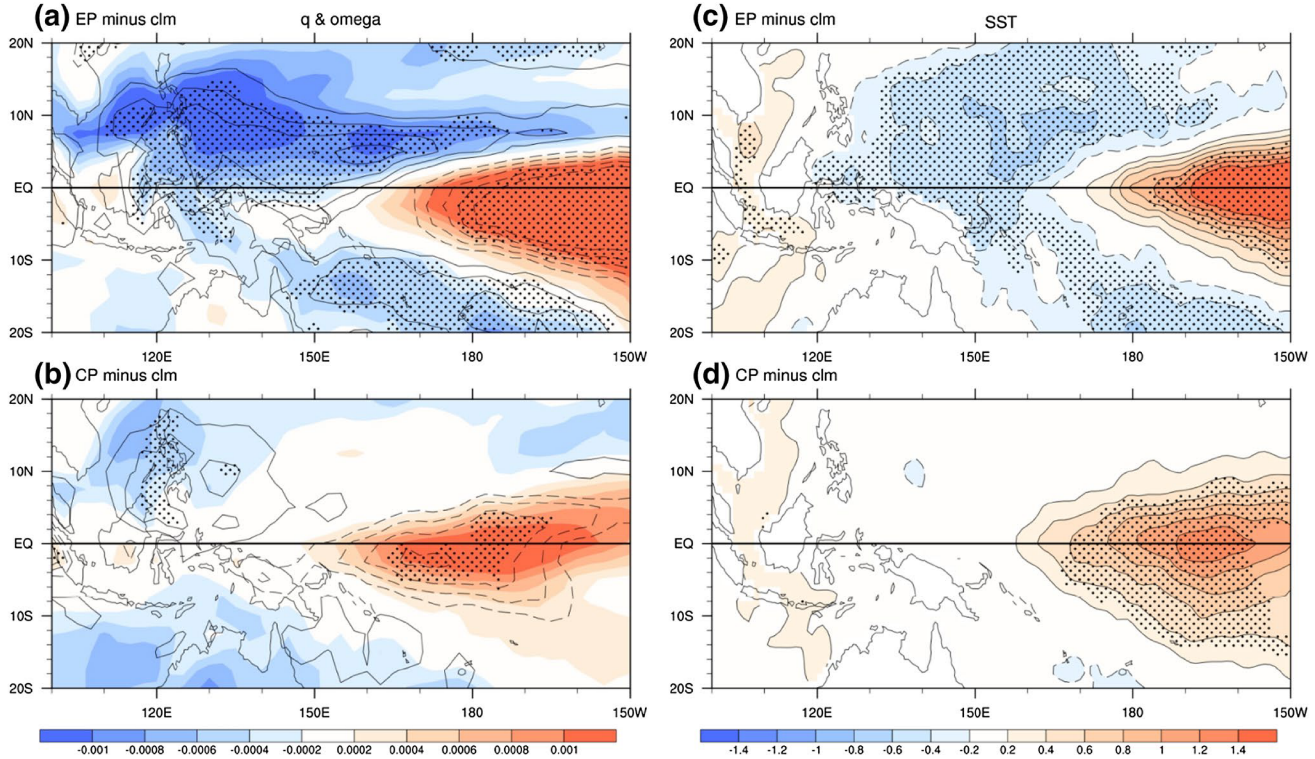

Fig. 16 Winter (November–April) mean 850-hPa specific humidity (kg kg^{-1}, shaded) and 500-hPa pressure velocity (Pa s^{-1}, contour), in which the climatology is removed, averaged over **a** EP El Niño winters and **b** CP El Niño winters. **c, d** are same as in **a, b**, but for SST. Results passing the significant test at 95% confidence level for pressure velocity and SST are stippled

in CP MJO is around two times as much as that in the EP MJO.

The stronger MSE tendency in the CP MJO is primarily attributed to three processes in meridional moisture advection anomalies. The first one is the advection of background moisture by intraseasonal meridional wind anomaly (i.e., $-v'\partial\bar{q}/\partial y$). This term has a positive contribution to the MSE tendency in both the CP MJO and the EP MJO as poleward wind anomalies off the equator act on the background moisture which maximizes near the equator. The smaller positive $-v'\partial\bar{q}/\partial y$ in the EP MJO is due to weaker v' in the northern hemisphere whereas their background moisture gradient are similar. The weaker v' is further related to weaker suppressed convection anomaly over the northern central Pacific.

The second process is the advection of intraseasonal moisture anomaly by background meridional wind ($-\bar{v}\partial q'/\partial y$). This term is near zero in the CP MJO while it is largely negative in the EP MJO. The more negative $-\bar{v}\partial q'/\partial y$ in the EP MJO is primarily due to larger negative moisture gradient over the northern hemisphere while the background wind fields are similar.

The third process is the nonlinear eddy advection ($-v''\partial q''/\partial y$). This term has a positive contribution to MSE tendency in both the CP MJO and the EP MJO. The larger positive advection term in the CP MJO is due to more suppressed high-frequency activity, which may be further modulated by the intraseasonal suppressed convection anomaly.

The amplitude in the intraseasonal suppressed convection anomaly over the central Pacific, which is critical to the three moisture advection processes, may be related to the mean moisture amount locally. The less mean moisture in the EP El Niño is possibly induced by stronger cold SST anomaly, which is in favor of descending motion anomaly. It is worth mentioning that such a physical mechanism needs to be verified through numerical experiments in future studies.

Acknowledgements This work was supported by National Key R&D Program 2017YFA0603802/2015CB453200, NSFC 41705059/41630423/41475084/41575043 /41405075, NSF AGS-1643297, Jiangsu project BK20150062 and R2014SCT00, JAMSTEC JIJI Theme 1 project and the Priority Academic Program Development of Jiangsu Higher Education Institutions (PAPD). This is SOEST contribution number 10245, IPRC contribution number 1290, and ESMC contribution 188.

References

Ashok K, Behera SK, Rao SA, Weng H, Yamagata T (2007) El Niño Modoki and its possible teleconnection. J Geophys Res Oceans 112:C11007

Bergman JW, Hendon HH, Weickmann KM (2001) Intraseasonal air–sea interactions at the onset of El Niño. J Climate 14:1702–1719

Chen L, Yu Y, Sun DZ (2013) Cloud and water vapor feedbacks to the El Niño warming: are they still biased in CMIP5 models? J Clim 26:4947–4961

Chen L, Yu Y, Zheng W (2016a) Improved ENSO simulation from climate system model FGOALS-g1.0 to FGOALS-g2. Clim Dyn 47:2617–2634. doi:10.1007/s00382-016-2988-8

Chen X, Ling J, Li C (2016b) Evolution of the Madden–Julian oscillation in two types of El Niño. J Clim 29:1919–1934

Chung P-H, Li T (2013) Interdecadal relationship between the mean state and El Niño types. J Clim 26:361–379

Dee DP et al (2011) The ERA-Interim reanalysis: configuration and performance of the data assimilation system. Q J R Meteorol Soc 137:553–597

Deng L, Li T, Liu J, Peng M (2016) Factors controlling the interannual variations of MJO intensity. J Meteorol Res 30:328–340

Duchon CE (1979) Lanczos filtering in one and two dimensions. J Appl Meteorol 18:1016–1022

Feng J, Li JP (2013) Contrasting impacts of two types of ENSO on the boreal spring Hadley circulation. J Clim 26:4773–4789. doi:10.1175/JCLI-D-12-00298.1

Feng J, Liu P, Chen W, Wang X (2015) Contrasting Madden–Julian oscillation activity during various stages of EP and CP El Niños. Atmos Sci Lett 16:32–37

Fink A, Speth P (1997) Some potential forcing mechanisms of the year-to-year variability of the tropical convection and its intraseasonal (25–70-day) variability. Int J Climatol 17:1513–1534

Gill AE (1980) Some simple solutions for heat-induced tropical circulation. Q J R Meteorol Soc 106:447–462

Gushchina D, Dewitte B (2012) Intraseasonal tropical atmospheric variability associated with the two flavors of El Niño. Mon Weather Rev 140:3669–3681

Gutzler DS (1991) Interannual fluctuations of intraseasonal variance of near-equatorial zonal winds. J Geophys Res Oceans 96:3173–3185

Hendon HH, Zhang C, Glick JD (1999) Interannual variation of the Madden–Julian oscillation during austral summer. J Clim 12:2538–2550

Hendon HH, Wheeler MC, Zhang C (2007) Seasonal dependence of the MJO–ENSO relationship. J Clim 20:531–543

Hsu P-c, Xiao T (2017) Differences in the initiation and development of Madden-Julian Oscillation over the Indian Ocean associated with two types of El Niño. J Clim. doi:10.1175/JCLI-D-16-0336.1 **(in press)**

Hung M-P, Lin J-L, Wang W, Kim D, Shinoda T, Weaver SJ (2013) MJO and convectively coupled equatorial waves simulated by CMIP5 climate models. J Clim 26:6185–6214

Kajikawa Y, Yasunari T (2005) Interannual variability of the 10–25- and 30–60-day variation over the South China Sea during boreal summer. Geophys Res Lett 32:L04710

Kessler WS, Kleeman R (2000) Rectification of the Madden–Julian oscillation into the ENSO cycle. J Clim 13:3560–3575

Kim D, Kug J-S, Sobel AH (2014) Propagating versus Nonpropagating Madden–Julian Oscillation Events. J Climate 27:111–125

Kim D, Sobel AH, Maloney ED, Frierson DMW Kang I-S (2011) A systematic relationship between intraseasonal variability and mean state bias in AGCM simulations. J Clim 24:5506–5520

Kiranmayi L, Maloney ED (2011) Intraseasonal moist static energy budget in reanalysis data. J Geophys Res Atmos 116:D21117

Lau K-M, Chan PH (1988) Intraseasonal and interannual variations of tropical convection: a possible link between the 40–50 day oscillation and ENSO? J Atmos Sci 45:506–521

Liebmann B, Smith CA (1996) Description of a complete (interpolated) outgoing longwave radiation dataset. Bull Am Meteorol Soc 77:1275–1277

Lin A, Li T (2008a) Energy Spectrum characteristics of boreal summer intraseasonal oscillations: climatology and variations during the ENSO developing and decaying phases. J Clim 21:6304–6320

Lin A, Li T (2008b) Energy spectrum characteristics of boreal summer intraseasonal oscillations: climatology and variations during the ENSO developing and decaying phases*. J Clim 21:6304–6320

Lin J-L et al (2006) Tropical intraseasonal variability in 14 IPCC AR4 climate models. Part I: convective signals. J Clim 19:2665–2690

Liu F, Li T, Wang H, Deng L, Zhang Y (2016) Modulation of boreal summer intraseasonal oscillations over the western North Pacific by ENSO. J Clim 29:7189–7201

Madden RA, Julian PR (1994) Observations of the 40-50-day tropical oscillation—a review. Mon Weather Rev 122:814–837

Maloney ED (2009) The Moist static energy budget of a composite tropical intraseasonal oscillation in a climate model. J Clim 22:711–729

McPhaden MJ, Lee T, McClurg D, 2011: El Niño and its relationship to changing background conditions in the tropical Pacific Ocean. Geophys Res Lett 38

Moon J-Y, Wang B, Ha K-J (2011) ENSO regulation of MJO teleconnection. Clim Dyn 37:1133–1149

Neelin JD, Held IM (1987) Modeling tropical convergence based on the moist static energy budget. Mon Weather Rev 115:3–12

Raymond DJ, Fuchs Ž (2009) Moisture modes and the Madden–Julian oscillation. J Clim 22:3031–3046

Rayner N, Parker D, Horton E, Folland C, Alexander L, Rowell D, Kent E, Kaplan A (2003) Global analyses of sea surface temperature, sea ice, and night marine air temperature since the late nineteenth century. J Geophys Res 108:4407

Ren H-L, Jin F-F (2011) Niño indices for two types of ENSO. Geophys Res Lett 38:L04704

Seiki A, Takayabu YN (2007) Westerly wind bursts and their relationship with intraseasonal variations and ENSO. Part I: Statistics. Mon Weather Rev 135:3325–3345

Sobel A, Maloney E (2013) Moisture modes and the Eastward propagation of the MJO. J Atmos Sci 70:187–192

Sobel AH, Nilsson J, Polvani LM (2001) The weak temperature gradient approximation and balanced tropical moisture waves. J Atmos Sci 58:3650–3665

Takahashi K, Montecinos A, Goubanova K, Dewitte B (2011) ENSO regimes: reinterpreting the canonical and Modoki El Niño. Geophys Res Lett 38:L10704. doi:10.1029/2011GL047364

Tang Y, Yu B (2008) MJO and its relationship to ENSO. J Geophys Res 113:D14106

Wang L, Chen L (2016) Interannual variation of convectively-coupled equatorial waves and their association with environmental factors. Dyn Atmos Oceans 76(Part 1):116–126

Wang L, Li T, Zhou T (2012) Intraseasonal SST variability and air–sea interaction over the kuroshio extension region during Boreal Summer*. J Clim 25:1619–1634

Wang L, Li T, Maloney E, Wang B (2017) Fundamental causes of propagating and non-propagating MJOs in MJOTF/GASS models. J Clim 30:3743–3769. doi:10.1175/JCLI-D-1116-0765.1171

Wheeler M, Hendon HH (2004) An all-season real-time multivariate MJO index: development of an index for monitoring and prediction. Mon Weather Rev 132:1917–1932

Wheeler MC, Kiladis GN (1999) Convectively coupled equatorial waves: analysis of clouds and temperature in the wavenumber–frequency domain. J Atmos Sci 56:374–399

Xiang B, Wang B, Li T (2013) A new paradigm for the predominance of standing Central Pacific Warming after the late 1990s. Clim Dyn 41:327–340

Yang J, Wang B, Wang B (2008) Anticorrelated intensity change of the quasi-biweekly and 30–50-day oscillations over the South China Sea. Geophys Res Lett 35:L16702

Zhang C (2005) Madden–Julian oscillation. Rev Geophys 43:RG2003

Zhang C, Gottschalck J (2002) SST anomalies of ENSO and the Madden–Julian oscillation in the equatorial pacific. J Clim 15:2429–2445

Zhou T, Wu B, Dong L (2014) Advances in research of ENSO changes and the associated impacts on Asian-Pacific climate. Asia Pac J Atmos Sci 50:405–422